


Influence of Neuronal Morphology on the Shape of Extracellular Recordings With Microelectrode Arrays: A Finite Element Analysis

Robert Bestel , Ursula van Rienen , Christiane Thielemann , and Revathi Appali 

Abstract—Objective: Measuring neuronal cell activity using microelectrode arrays reveals a great variety of derived signal shapes within extracellular recordings. However, possible mechanisms responsible for this variety have not yet been entirely determined, which might hamper any subsequent analysis of the recorded neuronal data. **Methods:** To investigate this issue, we propose a computational model based on the finite element method describing the electrical coupling between an electrically active neuron and an extracellular recording electrode in detail. This allows for a systematic study of possible parameters that may play an essential role in defining or altering the shape of the measured electrode potential. **Results:** Our results indicate that neuronal geometry, neurite structure, as well as the actual pathways of input potentials that evoke action potential generation, have a significant impact on the shape of the resulting extracellular electrode recording and explain most of the known variations of signal shapes. **Conclusion:** The presented models offer a comprehensive insight into the effect of geometrical and morphological factors on the resulting electrode signal. **Significance:** Computational modeling complemented with experimental measurements shows much promise to yield meaningful insights into the electrical activity of a neuronal network.

Index Terms—Simulation, MEA, FEM, Microelectrode, Extracellular potentials.

I. INTRODUCTION

ANALYZING the electrical activity of neuronal cultures offers the opportunity to investigate communication in

Manuscript received January 12, 2020; revised July 23, 2020 and September 3, 2020; accepted September 13, 2020. Date of publication September 24, 2020; date of current version March 19, 2021. This work was supported in part by the Bayrisches Staatsministerium für Bildung, Kultur, Wissenschaft und Kunst in the frame of ZEWIS and by Deutsche Forschungsgemeinschaft (DFG) under Grant AP 259/1-1 and SFB 1270/1- 299150580 (Corresponding authors: Robert Bestel; Revathi Appali.)

Robert Bestel is with the Biomems lab, Technische Hochschule Aschaffenburg, 68519 Viernheim, Germany (e-mail: robert.bestel@mailbox.org).

Ursula van Rienen is with the Institute of General Electrical Engineering, University of Rostock, the Department Life, Light & Matter, University of Rostock, and also with the Department Ageing of Individuals and Society, University of Rostock.

Christiane Thielemann is with the Biomems lab, Technische Hochschule Aschaffenburg.

Revathi Appali is with the Institute of General Electrical Engineering, University of Rostock, and also with the Department Ageing of Individuals and Society, University of Rostock, 18059 Rostock, Germany.

Digital Object Identifier 10.1109/TBME.2020.3026635

neuronal networks as well as the influence of various external stimuli. Compared to experiments *in vivo*, *in vitro* studies based on microelectrode arrays (MEA) often allow for more defined experimental setups. Electrical activity, i.e., neuronal action potentials (AP), can be either derived with standard MEA or using more recently developed high-density MEA (HD-MEA) that offer better spatial resolution [1], [2]. This data can be analyzed, e.g., in terms of global network activity, synchrony, or functional connectivity. Such methods rely on accurate detection of neuronal AP, also called spikes in their derived form that are present in a recorded signal. In the case of multiple neurons contributing to an electrode recording, each spike should be traced back to the cell that generated the respective AP to avoid errors in the subsequent data analysis. In this context, a complex issue arises, as measured spikes show significant shape variations [3], [4], while the origin of this phenomenon, as well as the relevant factors behind it, are still not entirely understood.

One possible approach to address this issue is via computational *in silico* models. Based on earlier neuron models [5]–[10], we have conducted a simulation study to evaluate the effect of neuron morphology on the resulting electric potentials in extracellular space during neuronal AP-generation and -propagation [11].

In analogous works, simulations reproduced the derivation of neuronal signals of cells *in vivo* [10], [12], [13], or of slice preparations [14], [15] using virtual or tip shaped electrodes or electrode arrays. In these models, a cable equation-based approach was used, and the electrode signals were calculated using point- and line-source approximation [10], [14], [15] or explicit three-dimensional electrode representations [12], [13].

An alternative to the cable equation is the description of neuronal signal generation and propagation using the electroquasistatic approximation of Maxwell's equations (EQS) (see [16]–[19]). It allows for a full three-dimensional representation of the neuron, as shown in the model presented in [20]. The study investigates various parameters affecting the derivation of electric signals of a single neuron in a three-dimensional *in vivo* domain using a silicon multi-electrode array.

For comparison, cable equation-based models generally allow for the simulation of larger neuronal structures and multiple neurons in small networks, as in *in vivo* or slice preparations. However, its applicability is fundamentally limited to symmetric rotational structures. Consequently, the accuracy of this approach decreases compared to the EQS-approach for small,

irregular geometries, as, e.g., neurons that are adherent on an extracellular surface or an MEA-electrode. Regarding electrode representation, probes for such cultures and the electric conditions of the surrounding experimental setup have significant differences for *in vitro*-based recordings using MEA with planar electrodes. In addition, point and line source approximation may not account for all possible effects of the setup in extracellular space, as possible interdependences may be omitted. For *in vitro* setups using MEA, the study of [21] simulates electric stimulation with a three-dimensional finite element method (FEM) model. Simulations of [9] reproduce the derivation of neuronal signals of a single cell using a planar MEA electrode, also using a 3D FEM model. These models generally impose no limitations on neuronal geometry and are advantageous for modeling *in vitro* cultures on MEA chips.

Nevertheless, computational complexity is much higher than cable equation-based descriptions and, therefore, imposed limitations on the description of neuron geometry. In this context, the computational model described here and in our previous work can be seen as improved and refined successors, utilizing the increase in computational capacity since then. In our previous computational study (see [11]), we have shown that both geometry and ion channel distribution significantly impact the extracellular action potential (EAP) that is created during neuronal AP-generation and subsequent -propagation. Furthermore, the simulations indicated that only minor geometric changes are necessary to affect the resulting extracellular potential distribution.

Since the geometry of the neuron determines the physical contact with an underlying surface, a suitable geometric approximation becomes crucial if the measurement of a neuronal AP using an extracellular MEA-electrode is to be reproduced within a mathematical model. For this purpose, the results of our previous work presented in [11] showed fundamental advantages of an electro-quasistatic-based (EQS) approach compared to a cable equation-based approach to describe neuronal AP-propagation. EQS allows for irregular geometric shapes and, therefore, for a much more accurate approximation of neuronal geometry.

In an attempt to extend our previous simulation model, in this work, we introduce an extracellular electrode to the neuron model and further refine the geometric and electrophysiological representation of the neuron.

The finite element method is used to describe the neuronal activity of a 3D neuron in an *in vitro* environment. Neuronal AP-generation is approximated with the Hodgkin-Huxley model and subsequent AP-propagation calculated using an EQS-based approach. Using this model-setup, the influence of electrode position concerning neuron geometry is evaluated and the effects of several parameters defining the electrical coupling between neuron and electrode are analyzed. Additionally, the influence of more complex neurite structures, as well as different origins to evoke neuronal AP-generation, are investigated.

Our results show that the signal shape measured by an extracellular electrode is highly dependent on its position to the neuron geometry. In addition, parameters such as neuron-electrode distance or electrode coverage, e.g., by packing glial cells, are found to have a significant influence on the measured signal

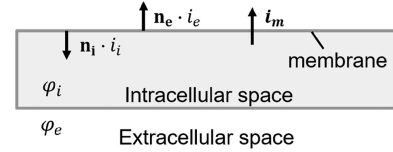


Fig. 1. Schematic drawing of the domain of the membrane model indicating respective mathematical parameters.

amplitude. Finally, we show that the actual path of the AP, as well as the origin of evocation that induced initial AP-generation, has an essential influence on the shape of the extracellular electrode recording.

II. MODEL DESCRIPTION

Regardless of the actual neuron geometry, three distinct mathematical aspects need to be tackled. One task is the calculation of the changing intracellular potential φ_i due to AP-generation and subsequent propagation (see Fig. 1).

Similarly, changes in the extracellular potential φ_e caused by neuronal electric activity need to be described. Finally, the ionic current i_m that is generated across the membrane during local AP-generation must be calculated. The transmembrane current i_m depends on the transmembrane potential φ_m , defined as $\varphi_i - \varphi_e$, and impacts the spatiotemporal evolution of the intra- and extracellular potentials φ_i and φ_e respectively. Consequently, a detailed description of the electrical activity, or in other words, the AP-generation along the neuronal membrane is crucial for accurate simulation.

A. Action Potential Generation With Adapted Hodgkin-Huxley Model

The Hodgkin-Huxley model is the most used mathematical approach to reproduce the AP-generation of neurons [22]. Its central equation describes the transmembrane current density i_m as the sum of ionic current densities i_{Na} , i_K and i_L and the capacitive change of transmembrane potential φ_m as

$$i_m = c_m \frac{d\varphi_m}{dt} + i_{ion} = c_m \frac{d\varphi_m}{dt} + i_{Na} + i_K + i_L. \quad (1)$$

Transmembrane current densities due to Na^+ and K^+ ions are described by the terms i_{Na} and i_K . The variable i_L combines a variety of secondary ions that only play a minor role. While the original model had been devised based on the electrophysiological properties of the giant squid axon, adapted models were proposed to capture the characteristics of mammalian neurons more accurately and take various temperature-dependent effects into account [23], [24]. Similar to the original model each of the current densities is quantified in mA per m^2 and generally calculated as

$$i_{Na}(T) = g_{Na}(T) m(T)^3 h(T) (\varphi_m - E_{Na}(T)), \quad (2)$$

$$i_K(T) = g_K(T) n(T) (\varphi_m - E_K(T)), \quad (3)$$

$$i_L(T) = g_L(T) (\varphi_m - E_L(T)). \quad (4)$$

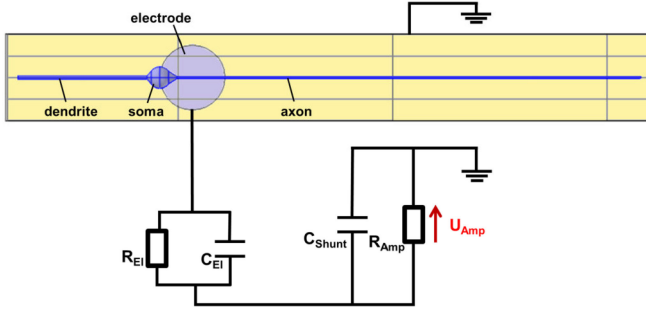


Fig. 2. Schematic of the connection between the FEM model and the equivalent circuit description of the extracellular electrode (top view).

The parameters E_{Na} , E_K and E_L describe the ion-channel-dependent reversal potentials and g_{Na} , g_K and g_L the electrical membrane conductivities for the respective ion channel. The ionic currents i_{Na} and i_K are further governed by time- and space-dependent gating variables m , h , and n , describing the opening state of the corresponding ion channel. For the adapted model, all these parameters are dependent on the temperature T with the respective equations (A1-A3) shown in the Appendix.

B. EQS-approach

For describing AP-propagation and potential distribution in extracellular space, a system of EQS-based equations is used. To this end, a form of the continuity equation is implemented in both intra- and extracellular domains [6], [7], [9], [11].

$$\nabla \cdot \left(\sigma_i \nabla \varphi_i + \varepsilon_0 \varepsilon_i \frac{\partial}{\partial t} \nabla \varphi_i \right) = 0, \quad (5)$$

$$\nabla \cdot \left(\sigma_e \nabla \varphi_e + \varepsilon_0 \varepsilon_e \frac{\partial}{\partial t} \nabla \varphi_e \right) = 0. \quad (6)$$

The neuronal membrane, which separates the two domains, is modeled using the thin-film approximation [9]. This means the membrane is not described as an additional volume domain but as two overlapping boundaries. On each boundary, a position-dependent Neumann condition is implemented, which defines the transmembrane current density i_m along the respective normal vectors \mathbf{n}_i and \mathbf{n}_e into intra- and extracellular space

$$\mathbf{n}_i \cdot i_i = \mathbf{n}_i \cdot \sigma_i \nabla \varphi_i = -i_m, \quad (7)$$

$$\mathbf{n}_e \cdot i_e = \mathbf{n}_e \cdot \sigma_e \nabla \varphi_e = i_m. \quad (8)$$

C. Outer Boundary Conditions and Electrode Description

For the outer boundary at the bottom of the extracellular domain, a Neumann zero boundary condition is applied to model the insulating glass surface of an MEA with normal vector \mathbf{n}_s

$$\mathbf{n}_s \cdot i_e = \mathbf{n}_s \cdot \sigma_e \nabla \varphi_e = 0. \quad (9)$$

A circular area is defined on this surface representing the metal layer of an MEA electrode (see Fig. 2).

An electrical equivalent circuit based on previous mathematical models of [25], [26] describes the boundary condition of this electrode surface. The circuit capacitance C_{El} and resistance

TABLE I
GEOMETRICAL DIMENSIONS OF MODELS I-III

Quantity	Value
Soma diameter [27], [28]	10 μm
Axon diameter [29], [30]	1 μm
Axon hillock initial/end diameter	3 μm / 1 μm
Dendrite diameter [27], [30]	1.5 μm
Dendrite tapering initial/end diameter	1.5 μm /3 μm

R_{El} describe the impedance of the electrode and the electrical double layer on top of the electrode surface. The capacitance C_{Shunt} accounts for losses across the MEA transmission lines. Finally, the resistance R_{Amp} defines the input resistance of the operational amplifier of the subsequent measuring system. The values of the elements in the equivalent circuit are taken from [26], with $R_{El} = 10 \text{ k}\Omega$, $C_{El} = 0,63 \text{ nF}$, $R_{Amp} = 100 \text{ G}\Omega$ and $C_{Shunt} = 20 \text{ pF}$.

On the remaining outer boundaries, a Dirichlet zero condition is used to account for the reference electrode of the MEA, which sets the extracellular potential to zero.

$$\varphi_B = 0. \quad (10)$$

To create a complete electrical circuit, the respective zero potential condition is also defined for the description of the electrode circuit.

D. Model Geometry and Electrophysiology

To evaluate the influence of neuronal geometry, three different neuron models, I-III were created with increasing complexity. The general geometric parameters, such as soma diameter or axon and dendrite radius, were defined based on values presented in previous publications (see Table I). General electrophysiological values of the neuron and electrical parameters of the extracellular medium were similarly taken from corresponding literature (see Table II).

Model I consists of a simplified neuron geometry describing an adherent neuron on an MEA surface (see Fig. 3). The distance between the glass surface and the neuron is defined homogeneously as 100 nm [31]. The neuron model is generally comprised of geometric primitives, cylindrical for neurites, and spherical for the soma, while axon hillock and tapering from soma to dendrite are based on conical structures.

These basic shapes are modified to approximate adherence of the cell on the glass substrate. To limit computational complexity, we imposed a homogeneous or flat adhesion, and any form of focal adhesion was not accounted for in our models (see, e.g. [31]–[34]).

The surrounding extracellular space is defined as a cubic section of extracellular medium with electrical parameters of saline solution. Different densities of Na^+ and K^+ ion channels are imposed for each part of the neuron, e.g., soma, axon initial segment (AIS), and dendrite (see Table II). At the interface of two neuronal subdomains, the transition of the different ion channel densities is modeled with a sigmoid function [11]. While most ion-specific membrane conductivities are identical to the model

TABLE II
GENERAL ELECTROPHYSIOLOGICAL PARAMETERS USED IN MODELS I-III

Symbol	Description	Value
c_m	Specific membrane capacitance [24]	10 nF/mm ²
r_m	Specific membrane resistance [24]	1/3 MΩmm ²
r_l	Specific intracellular resistance [24]	1 kΩmm
E_{Na}	Reversal potential of the Hodgkin-Huxley model for sodium ions [24]	50 mV
E_K	Reversal potential of the Hodgkin-Huxley model for potassium ions [24]	-77 mV
E_L	Reversal potential of the Hodgkin-Huxley model for leakage current ions [24]	-54 mV
g_{Na}	Specific conductivity of the axon, axon hillock and soma for sodium ions [6]	20 mS/cm ²
g_K	Specific conductivity of the axon, axon hillock and soma for potassium ions [6]	20 mS/cm ²
g_{NaAIS}	Specific conductivity of the AIS for sodium ions [6]	120 mS/cm ²
g_{KAIS}	Specific conductivity of the (AIS) for potassium ions [6]	36 mS/cm ²
g_{Naden}	Specific conductivity of the dendrite for sodium ions (adapted from [6])	3 mS/cm ²
g_{Kden}	Specific conductivity of the dendrite for potassium ions (adapted from [6])	1 mS/cm ²
g_L	Specific conductivity of the neuron for leakage current ions [9]	0.3 mS/cm ²
φ_{init}	Initial potential of soma, axon, and dendrite	-65 mV
$\varphi_{initAIS}$	Initial potential of AIS	-46 mV
m_{init}	Initial value of m (altered value in AIS)	0.05 (0.4)
h_{init}	Initial value of h	0.6
n_{init}	Initial value of n (altered value in AIS)	0.32 (0.36)
σ_i	Conductivity of the intracellular medium [22]	1 S/m
σ_e	Conductivity of the extracellular medium [22]	0.3 S/m
ϵ_i	Relative permittivity of the intracellular medium (~ value of water)	88
ϵ_e	Relative permittivity of the extracellular medium (~ value of water)	88

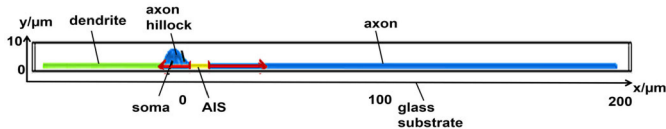


Fig. 3. Schematic drawing of model I (side view). The colors indicate different ion channel densities of the membrane (see Table II).

of [6], values along the dendrites are slightly adapted to the ion channel kinetics of the temperature-dependent model modified for mammalian neurons presented in [24]. Initial AP-generation is induced at the AIS along the initial 10 μm of the axon. This is done by altering the initial values of the intracellular potential φ_i as well as the local ion channel gating parameters m , n , and h . Such a method has the advantage that possible artifacts caused by external current or voltage based stimulation can be avoided.

Model II features a refined neuron geometry with more realistic neurite patterns and multiple branches (see Fig. 4). The neuron shape is generated artificially, yet based on camera lucida-based representations in the literature of typical neuron geometries (see, e.g. [35]). For better comparison with model I, the geometry of model II approximates the shape of a bipolar neuron. The dimensions of soma, axon, and dendrites, including

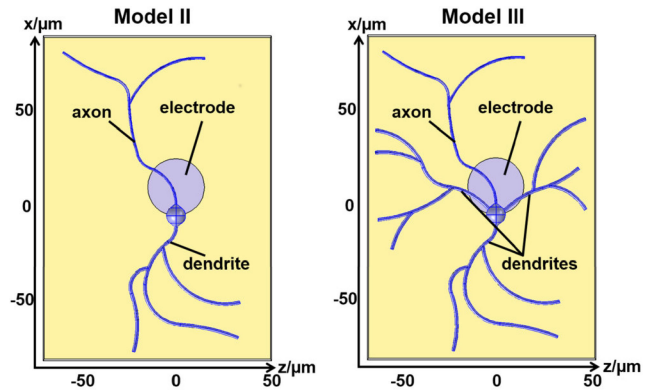


Fig. 4. Schematic drawing of models II and III (top view).

the conical connections, are not altered compared to model I. Likewise, electrophysiological properties, such as ion channel distribution and electrical membrane parameters, as well as starting values of the AIS for initial AP-generation remain unchanged.

For **Model III**, the geometry is further expanded by additional basal dendrites in order to reproduce the typical shape of a cortical pyramidal neuron, as shown in [35] (see Fig. 4). Similar to model II, all general geometrical and electrical properties are kept constant in order to accurately analyze the effect of neurite geometry on derived electrode signals.

E. Computation

All models were created and simulated using the software COMSOL Multiphysics® 5.2 (COMSOL AB, Stockholm, Sweden). For spatial discretization, a tetrahedral mesh with second-order Lagrange elements was used. The discretization of time-dependent quantities was done with an adaptive backward differentiation formula (BDF) scheme. Depending on the approximate error of discrete solution in previous time steps, both the order of the BDF scheme and the size of the time step could be altered by the software for each iteration up to a maximum order of three and a maximum step of 10 μs . Nonlinearities in the resulting system were addressed using Newton's method. Then, the linearized system was solved for each time step with the direct solver PARDISO using an allowed error tolerance of $1 \cdot 10^{-6}$. Simulations were carried out on a PC with two Intel Xeon E5-2687W v4 CPU with 24 cores, 256GB RAM, and a 64-bit operating system.

III. RESULTS

The initial analysis regarding the effect of parameters, such as neuron-electrode distance or electrode size on the resulting extracellular potentials and the respective electrode signals, is conducted on model I. Subsequently, Models II and III are used to evaluate the general effect of neuron geometry onto derived electrode signals. Furthermore, the influence of different stimulus origins necessary to provoke AP-generation at the AIS is assessed based on the geometry of model III.

TABLE III
MESHING AND COMPUTATION TIME OF MODELS I-III

Model	DOF (with glial layer)	Computation time (with glial layer)
Model I	403,000 (740,000)	18 h (35 h)
Model II	840,000 (-)	31 h (-)
Model III	1,740,000 (2,556,000)	35 h (90 h)

To ensure precise simulation, convergence concerning spatial and temporal discretization was determined for all models (see Table III). Because of their more complex geometries, the extended Models I and III with additional glial layer required significantly higher degrees of freedom (DOF) for spatial discretization. For temporal discretization, a time step of $10 \mu\text{s}$ was found to be sufficient for all models.

Considering computation time, model I was solved within 18 h while results for the more complex Models II and III were calculated within 31 h and 35 h, respectively. Again, computation times of the extended Models I and III with included glial layer coverage significantly increased to 35 h and 90 h. This is not only due to the increased spatial DOF but also due to the higher complexity of the resulting equation system, which is increased by the additional boundary conditions at the glial cell membranes.

To facilitate the model description, a general reference position was defined for the MEA-electrode. It is positioned so that the center of the electrode has an offset of $15 \mu\text{m}$ to the center of the soma in the x-direction (see Fig. 2). Any deviation from this reference position is explicitly described for the respective simulation.

A. Simplified Neuron Geometry (Model I)

The first step in analyzing the results of model I is the evaluation of the resulting intra- and extracellular potentials during AP-generation and subsequent propagation. While the general properties and results of the individual modeling approach have been discussed extensively in our previous work [11], a brief overview, as well as the effects of the newly included extracellular electrode, are given in the following.

Based on the initial conditions, the AP is first generated in the AIS and then propagates along the axon (see Fig. 5). By using the modified Hodgkin-Huxley model of [24] at a temperature of $37 \text{ }^\circ\text{C}$, a propagation velocity of $\sim 100 \text{ mm/s}$ is achieved. Furthermore, so-called back-propagation occurs with the AP being transmitted in the opposite direction into axon hillock, soma, and dendrite [36], [37], [38].

In extracellular space, the most noticeable potentials are created during AP-propagation through the soma. The amplitude of these potentials is negative near axon hillock and AIS, whereas positive amplitudes are seen at the opposite side of the soma (see Fig. 5). In short, this can be explained by the altered behavior of the ion channel kinetics at soma and axon hillock due to the change in diameter of intracellular space.

This causes a more pronounced Na^+ influx near the axon hillock and an increased K^+ current near the junction of soma and apical dendrite (for details see [11]). In contrast, a uniformly

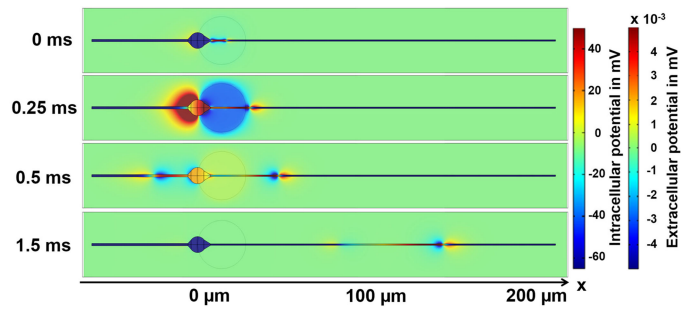


Fig. 5. Intra- and extracellular potentials of model I. The electrode is positioned with an offset of $15 \mu\text{m}$ from the electrode center to the center of the soma (top view). Initiated in the AIS, the AP propagates along the axon in the x-direction as well as back into soma and dendrite. Shifts in the extracellular potential near the recording electrode during AP-propagation yield time-dependent changes of the electrode potential. Due to the high conductivity of the electrode, there is no significant potential gradient across the electrode surface at any given point in time.

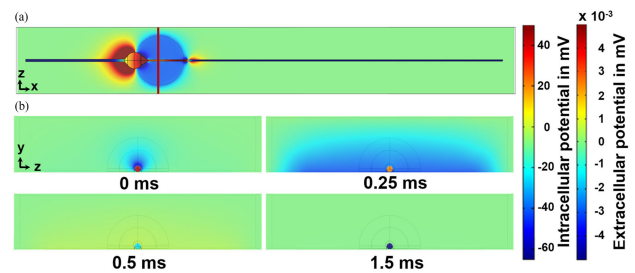


Fig. 6. Time-dependent potential distribution near the extracellular electrode of model I in front view with the electrode position indicated in (a). (b) A change in electrode potential caused by the electrical activity of the neuron yields a noticeable potential distribution in extracellular space, with values decreasing asymptotically towards the electrical ground, imposed at the top and side boundaries of the model.

shaped bipolar potential distribution is created in extracellular space during AP-propagation along axon and dendrite. As can be seen best at 0.25 ms, an iso-potential is created across the planar electrode surface for each point in time (see Fig. 6).

The observed iso-potential is caused by the high conductance of the metal electrode and shows the significant influence of the MEA-electrode on the extracellular potential in its vicinity. Due to the electrical properties of the extracellular medium and the boundary conditions in extracellular space, a time-varying potential distribution can be observed between the electrode and the reference potential at the outer boundaries of extracellular space. Hence, a change in electrode potential, caused by the electrical activity of the adherent neuron, affects not only the entire electrode surface but also the potential distribution of the surrounding area in extracellular space.

Based on the inhomogeneous evolution of the extracellular potential seen in fig. 6, the derived voltage signals vary significantly with electrode position (see Fig. 7). To highlight various shapes recorded for different electrode positions, y-axis scales are adapted for the shape types, which is emphasized by different line colors. In correspondence with respective extracellular potentials, electrode positions along axon and dendrite (red) yield small bipolar electrode signals.

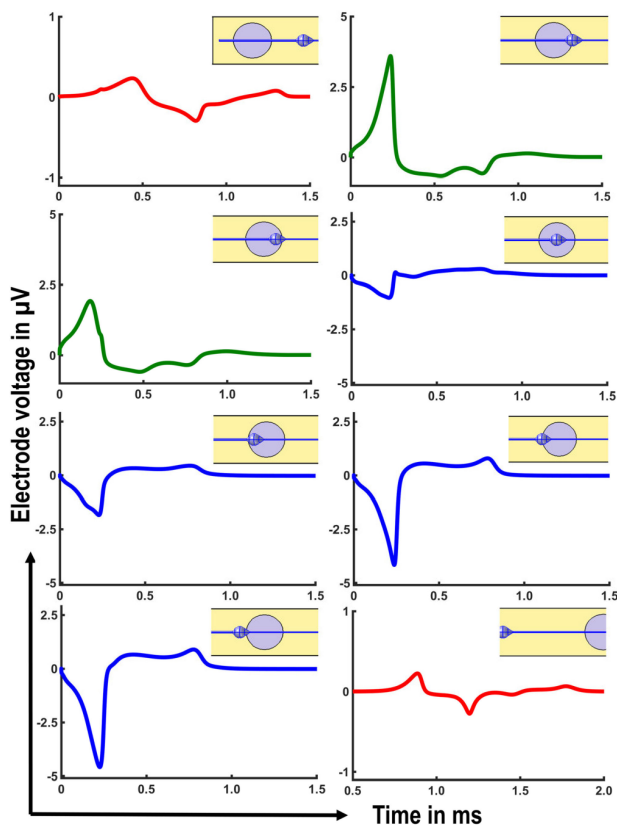


Fig. 7. Electrode voltage at different recording sites along the neuron geometry of model I. The line colors indicate a different scale of the y-axis to improve visibility of each signal shape. Traces along axon and dendrite show a bipolar shape with amplitudes below $\pm 1 \mu\text{V}$. In contrast, signals recorded near the soma have noticeably higher amplitudes with values close to $\pm 5 \mu\text{V}$. Whereas traces recorded between soma and dendrite show a predominant positive amplitude, this is reversed on the opposite side of the soma near AIS and axon.

Near the soma, however, derived signals show noticeably different shapes with predominant negative amplitudes near AIS and axon hillock (blue) and positive amplitudes near the junction of soma and dendrite (green). With values of $\pm 5 \mu\text{V}$ signal amplitudes around the soma are noticeably higher than amplitudes measured along the neurites, which do not exceed $\pm 1 \mu\text{V}$.

In comparison with [9], the electrode signal near the axon hillock shows a general agreement regarding signal shape and amplitude. However, the timescale of the signals in [9] with a duration of ~ 5 ms is significantly different compared to ~ 1 ms for model I. This difference can be explained by the usage of the adapted kinetics of mammalian ion channels from [24] in model I compared to the original kinetics of the Hodgkin-Huxley model [22] applied in [9]. Furthermore, the adapted geometry of our model offers a better representation of an adherent neuron and can explain additional differences.

In this context, it is somewhat surprising that signal amplitudes are in good agreement since the distance between neurons and electrodes is generally more than ten times higher in the model of [9] compared to our model, which calls for further investigation.

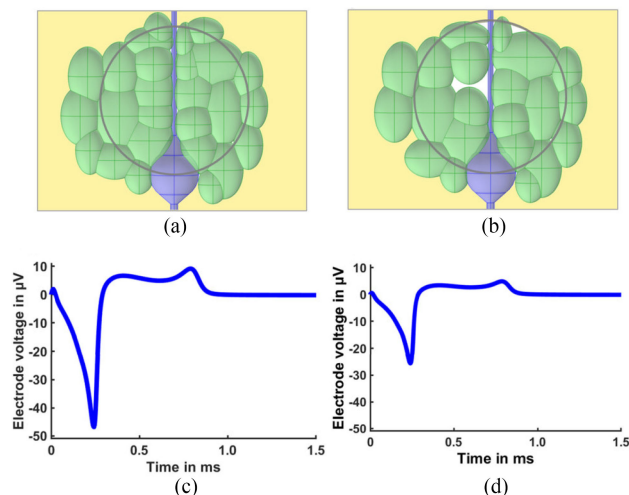


Fig. 8. Effect of a glial layer on the amplitude of derived electrode signals. The glial layer (green) in (a) fully covers the electrode surface (outlined in grey), whereas the layer that is shown in (b) features some small voids (white areas). (c) and (d) While a full glial coverage yields an increase of the derived signal amplitude by approximately one order of magnitude, the effect is noticeably mitigated even by few voids inside the layer. The signal shape is not affected in either case.

In contrast to [9], our model also allows for the simulation of electrode signals along the dendrite, offering an expanded analysis. However, in comparison with typical MEA-recordings, all simulated signals are generally about one order of magnitude smaller, as measured voltages have typical values around $\pm 30 - 100 \mu\text{V}$ (see [3], [26]). This significant difference calls for further investigation regarding this deviation between model and experimental results. Therefore, the possible reasons for this are analyzed in the following.

Compared to the geometry of model I, which is only comprised of a single neuron to reduce computational complexity, *in vitro* cultures consist of a whole network of neurons often surrounded by a layer of supporting cells. Based on the results shown in fig. 6, one can assume that an additional cell layer significantly alters the potential distribution generated between the electrode surface and the reference potential at the outer boundaries of extracellular space. Such additional coverage changes the electric resistance between the electrode surface and the extracellular reference potential at the outer boundaries, which consequently leads to a higher electric potential at the electrode. Hence, the amplitude of the derived electrode signal is increased.

B. Effect of Insulating Glial-Layer on Signal Amplitude

For verification of a possible influence of electrode coverage on the amplitude of extracellular recordings, model I is altered so that a layer of glial cells additionally covers the surface of the MEA-electrode (see Fig. 8).

Such cells are generally not considered to have an electrical activity similar to neurons [39], yet fulfill a supporting role in neural tissue and are also present in many *in vitro* cultures [40].

The introduced glial-layer is comprised of several ellipsoid-shaped cells with semi-axes ranging between $2-7 \mu\text{m}$. Each glial

cell is modeled with a resting potential of -90 mV, a passive cell membrane with a specific capacity $c_{m_{glia}}$ of $0.75 \mu\text{F}/\text{mm}^2$ and a specific leakage conductivity $g_{L_{glia}}$ of $1 \cdot 10^{-5} \text{ S}/\text{m}^2$ [41]. An electrode position with an offset of $15 \mu\text{m}$ (to the center of the soma in the x -direction) is chosen as reference. In agreement with previous results, a dense glial layer dramatically increases the resulting electrode signal amplitude by almost one order of magnitude to $-45 \mu\text{V}$ (see Fig. 8a and 8c).

The 100 nm small gap that is formed by the electrode surface and glial layer in y -direction significantly increase the electric resistance between the electrode surface and extracellular mass potential. In consequence, the amount of electric current transmitted to the input impedance of the amplifier stage during the electrical activity of the adherent neuron is increased, while the amount of leakage current to the outer boundaries of extracellular space decreases, respectively.

Hence, a noticeably higher electrode signal amplitude is achieved in case of additional electrode coverage. In addition, it can be shown that even small voids inside the layer cause a significant drop in amplitude (see Fig. 8b and 8d). However, the shape of the signal trace remains unaffected in both cases.

Overall, the results of the modified model I verify that electrode coverage is a highly important factor. Non-covered areas of the electrode surface yield noticeable leakage currents, which significantly influence the amplitude of the derived electrode signal. Reasonable signal amplitudes that are comparable with measured *in vitro* data can be achieved however, when a dense coverage of the electrode with an additional glial layer is imposed. The results highlight the importance of electrode coverage for the electric coupling between neurons and electrode, as reported in [20] and [21].

C. Effect of Neuron-Electrode Distance and Electrode Size

As the simulations based on model I have shown, both the shape and amplitude of the derived electrode signal are highly dependent on electrode position and neuron geometry (see Fig. 7). The impact of a possible offset in the z -direction, an increase in neuron-electrode distance in the y -direction, or the size of the MEA-electrode has not yet been investigated for the computational model. In the following, these three factors are addressed in a parameter study, and three particular situations of neuron-electrode coupling are evaluated:

Electrode setup 1: A planar MEA-electrode without additional electrode coverage

Electrode setup 2: A planar MEA-electrode with additional electrode coverage by a dense glial-layer (see Fig. 8a)

Electrode setup 3: A recessed MEA-electrode with a passivation layer typical for many MEAs (see e.g. [1], [26] or [42]). The layer material can be, e.g., SiO_2 , Si_3N_4 , or SU-8 photoresist with a thickness between $\sim 0.5 \mu\text{m}$ and several micro-metres. For an exemplary investigation, we modelled a passivation layer of $1 \mu\text{m}$ thickness, which creates a cavity at the electrode site. The electrical properties of an ideal insulator were chosen. No additional electrode coverage is imposed.

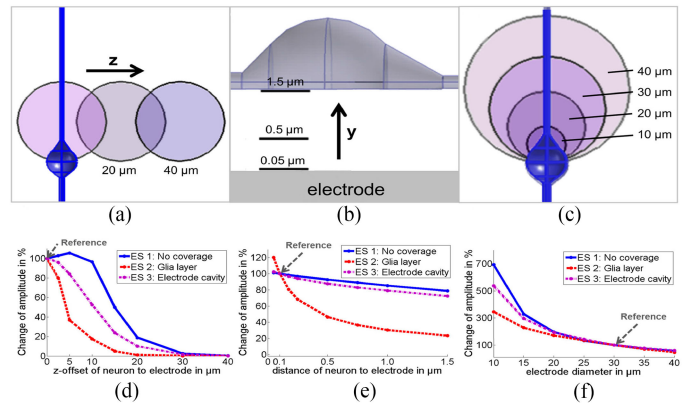


Fig. 9. Evaluation of the influence of electrode displacement (a), neuron-electrode distance (b) and electrode size on the derived signal amplitude (c). (d) In all of the three electrode setups (ES), the signal amplitude decreases dramatically with electrode displacement. The minor amplitude increase for a displacement of $5 \mu\text{m}$ in setup 1 can be explained by the extracellular potential distribution near the soma. (e) For electrode setup 2, the derived signal amplitude decreases asymptotically with a more considerable distance of the neuron to the electrode. Due to the generally smaller signal amplitudes, the effect is noticeably weaker in case of setups 1 and 3, respectively. (f) Signal amplitudes generally decrease with larger electrode diameter in all cases. Due to better conduction to the electrical ground in extracellular space, this effect is most pronounced for electrode setup 1.

The previously used reference position of the electrode is retained with an offset of $15 \mu\text{m}$ in the x -direction to the center of the soma and a distance of 100 nm between the cell membrane and the electrode surface. Based on this reference position, the recessed electrode in electrode setup 3 yields a signal amplitude of $-5.02 \mu\text{V}$ compared to $-4.58 \mu\text{V}$ for electrode setup 1 and $-45 \mu\text{V}$ for electrode setup 2 with additional glial layer coverage. The recessed electrode produces slightly higher signal amplitudes due to the small increase in electric resistance between the electrode surface and the reference potential at the boundaries of extracellular space compared to electrode setup 1. In the following parameter study, these voltages serve as a reference for each electrode setup, and the relative change of signal amplitude is evaluated (see Fig. 9).

The signal amplitudes generally decrease asymptotically for all setups with increasing electrode offset in the z -direction (see Fig. 9d). Similar to previous results, the signal shape remains to be generally unaffected. However, the amplitude decrease differs between the models, with electrode setup 2 showing the steepest decline. Signal amplitude decreases to less than 10% of the reference amplitude at an offset of $15 \mu\text{m}$, as the effect of additional electrode coverage is quickly lost for higher offsets.

Electrode setup 3 displays a slower reduction in signal amplitude, decreasing to $\sim 10\%$ at $20 \mu\text{m}$, and electrode setup 1 shows the slowest decline, reaching values below 10% of the original amplitude only well after a displacement of $20 \mu\text{m}$. In addition, the curve of electrode setup 1 shows a slight increase in the signal amplitude of 5% for smaller displacements around $5 \mu\text{m}$. This effect is due to the circular shape of the electrode in combination with the potential distribution near the neuron's soma. While the positive potential generated near the connection

between dendrite and soma is still partially captured for the reference electrode position, this already changes with small displacement in the z -direction. In consequence, the potential average across the electrode surface yields slightly higher negative amplitudes. However, this behavior is only visible due to the overall small signal amplitude of electrode setup 1 and cannot be seen in the two alternative setups.

Overall, all electrode setups generally show the expected decrease in amplitude in the case of a positional electrode displacement in the z -direction, which corresponds to more considerable distances between cell and electrode. Nonetheless, it is most evident for electrode setup 2, further highlighting the influence of current leakage due to an uncovered electrode surface. With respect to the model differences, results are in good agreement with previous findings shown in [13] and [21], showing a similar decrease in signal amplitude with further electrode displacement.

Furthermore, the cavity of electrode setup 3 makes it less susceptible to minor electrode displacement, even though not providing significantly higher signal amplitudes in general. Considering higher distances of the cell membrane to the electrode surface in the y -direction, e.g., due to insufficient cell adhesion, electrode setups 1 and 3 yield a nearly linear decline with increasing distance (see Fig. 9e).

In contrast, additional glial-coverage in electrode setup 2 leads to an asymptotic decline. In agreement with the previous results, this indicates that in setups 1 and 3, most of the electric current generated during AP-generation gets lost due to leakage currents rather than being transmitted to the input resistance of the amplifier. In consequence, increasing the distance between neuron and electrode and hence decreasing the electric resistance between the electrode surface and the reference potential only has a marginal effect.

However, it has to be noted that the small effect of the distance between neuron and electrode for setups 1 and 3 is mainly caused by the low amplitude of the electrode signal for the reference positions. The slow decrease in electrode voltage with increasing distance between neurons and electrode for setup 1 also explains the good agreement of results compared to findings shown in [9].

With the additional glial-layer coverage in electrode setup 2, however, signal amplitudes not only decrease more realistically with distance but also increase more significantly by more than 20% if the neuron-electrode distance is decreased to $0.05 \mu\text{m}$. The much steeper decline seen for electrode setup 2 is in good agreement with the results of [13]. Investigating the effect of different electrode sizes on the derived electrode signal amplitudes yields generally similar results for all three tested setups (see Fig. 9f).

With a diameter of $30 \mu\text{m}$ as a reference, signal amplitudes overall increase noticeably for smaller diameters, while decreasing with larger electrode sizes. This increase is most significant for setup 1, yielding an amplitude that is almost seven times higher for an electrode diameter of $10 \mu\text{m}$.

For electrode setup 3, the signal amplitude is about 540% of the reference value, whereas setup 2 only shows an increase to 350%. The different behavior of the electrode setups can again be explained by the leakage current that occurs in the case of

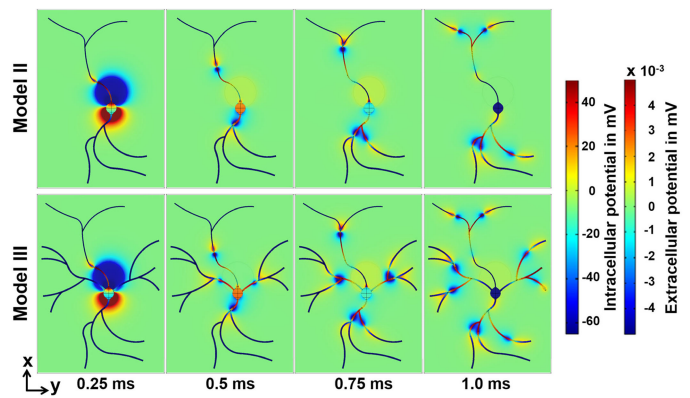


Fig. 10. Intra- and extracellular potentials of Models II and III (top view). Similar to model I (see Fig. 5), the AP propagates in the x -direction along the axon as well as back into soma and dendrite for both models. AP-propagation occurs similarly in both Models II and III, yet the additional dendritic structures of model III change the extracellular potential distribution in their vicinity.

uncovered electrode surfaces. The ratio between the areas of the electrode surface covered by the neuron itself and the non-covered area is reduced when the electrode size is decreased (see Fig. 9c). This yields higher resistance to the reference potential at the outer boundaries of extracellular space and, thus, a lower leakage current. In consequence, the amplitude of the resulting electrode signal increases with smaller electrode diameters. In addition, since the amplitude loss due to leakage is highest in the case of electrode setup 1, the effect of electrode size is most noticeable for this setup.

Compared with literature, the results are in good agreement with previous findings shown for planar electrodes presented in [9] and [21], as well as for electrodes for *in vivo* measurements simulated in [12], [13] and [20].

D. Physiological Neuron Geometry (Models II and III)

After a general analysis of the neuron-electrode coupling by employing model I, the neuron geometry is revised by introducing Models II and III. Both models feature shapes that are physiologically realistic and have multiple dendrites and axon branches, as shown for cortical neurons in [35]. The complex geometries of Models II and III and a comparison with the simplified model I, allow for a comprehensive evaluation of the effect of neuron shape on the derived electrode signal.

In a first step, AP-generation is initiated similar to model I in the AIS of Models II and III. Subsequent AP-propagation along the axon as well as back-propagation into soma and dendrites occurs essentially identical in both models (see Fig. 10). Similar electric potentials are observed in extracellular space despite the geometric differences. Overall, results are in good agreement with model I (see Fig. 6).

The AP spreads into each of the neurite branches at the branching points and is consequently regenerated for further propagation. This causes higher extracellular potentials near these points, as additional ionic currents are required to ensure AP-propagation in all subsequent pathways. Considering the

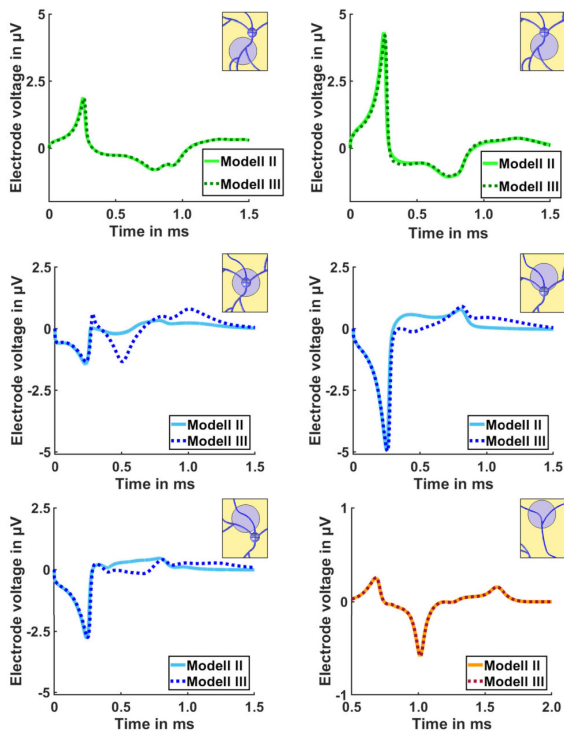


Fig. 11. Electrode voltages are derived at different recording sites on the neuron geometry of model II (solid line) and model III (dashed line). The line colors indicate a different scale of the y-axis to improve the visibility of each signal shape. While yielding mostly identical traces, the derived signal shapes differ near the soma, as the basal dendrites of model III generate additional ionic currents that alter the extracellular potential in this area.

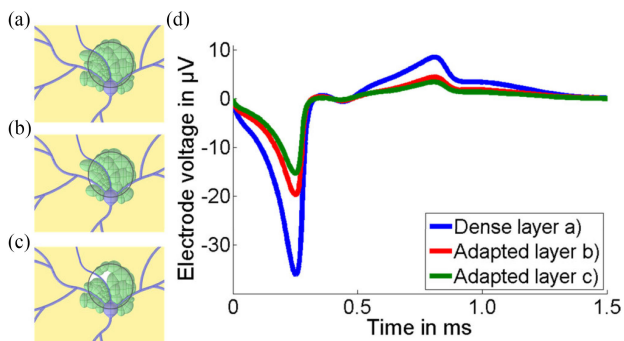


Fig. 12. Derived electrode signals for model III with different glial layer setups, as shown in (a)–(c). (d) In the case of dense electrode coverage, the signal amplitude is increased to $-36 \mu\text{V}$, which is more than five times higher compared to the original setup (see Fig. 10). Similar to model I even small voids inside the glial layer result in a significant decrease of signal amplitude. The signal shape, on the other hand, is not affected by either size or exact location of the voids.

derived electrode potential traces at various recording locations, Models II and III show similar signals (see Fig. 11).

Similar to fig. 7, the y-axis is adapted for different signal shape types, which are highlighted by varying line colors. Differences between the electrodes' signal traces of the two models are found at positions close to the soma. These deviations are caused by the additional basal dendrites of model III that provide additional

transmembrane currents and thus alter the extracellular potential in this area.

Due to the same effect, electrode signals derived near branching points show increased amplitudes when compared to regular recording sites along axon and dendrite. In comparison with respective signals calculated using model I, results are generally in good agreement in both shape and amplitude for respective electrode locations (see Fig. 5). In principle, all models yield electrode signals with negative amplitude near the axon hillock. Positive signal amplitudes are generated in the transition area of soma and apical dendrite. Along neurites, the extracellular electrode records a smaller, bipolar signal trace.

Additional neurite branches like the basal dendrites of model III alter the derived signal shapes, as they provide additional ionic current sources and change the distribution of the local extracellular potential.

Considering the amplitudes of derived electrode signals, values for Models II and III again do not exceed $\pm 5 \mu\text{V}$. This can be explained consequently, by imposing an additional glial layer, signal amplitudes are enhanced by about one order of magnitude (see Fig. 12). Another aspect shown with the results of model III is that voids inside the glial layer affect mainly the amplitude of the recorded electrode signal but do not significantly change signal shapes. The exact location of the voids, e.g., near the basal dendrites in contrast to near axon hillock or soma, does not alter the shape of the signal.

E. Origin of Stimulating Signal to Evoke AP-Generation

In all previous simulations, AP-generation and subsequent propagation were initialized in the AIS as spontaneous activity. Nonetheless, AP-generation is often evoked by incoming stimuli from surrounding neurons transmitted via the dendritic tree. Unlike the Models I and II, Model III offers different neurite pathways and input combinations to evoke AP-generation in the AIS. To analyze any effect of the origin of evocation on the resulting electrode signal, model III is simulated with four different input signal scenarios (see Fig. 13).

AP propagation is initialized using a time-dependent potential trace as a boundary condition at the end of several dendrites. The potential trace is generated by the modified Hodgkin-Huxley model using the ion channel densities of the dendrite (see Table II) and mainly describes an incoming AP at the given boundary (see Fig. 15). For all scenarios, the reference electrode position with an offset of $15 \mu\text{m}$ in x -direction relative to the center of the soma is maintained.

In the case of scenario 1, this boundary condition is solely imposed on the branches of the apical dendrite (see Fig. 13a). However, even though propagating along the dendrite simulation results show that the dendritic potential is unable to depolarize the larger volume of the soma and consequently AP-generation in the AIS fails. The failure can be explained by the sudden increase of intracellular volume at the junction of dendrite and axon, which can cause failing AP-propagation (see [43]). In this context, the geometry at the junction between basal dendrite and soma is altered for scenario 2 to create a more gradual expansion of intracellular volume. After geometric alteration,

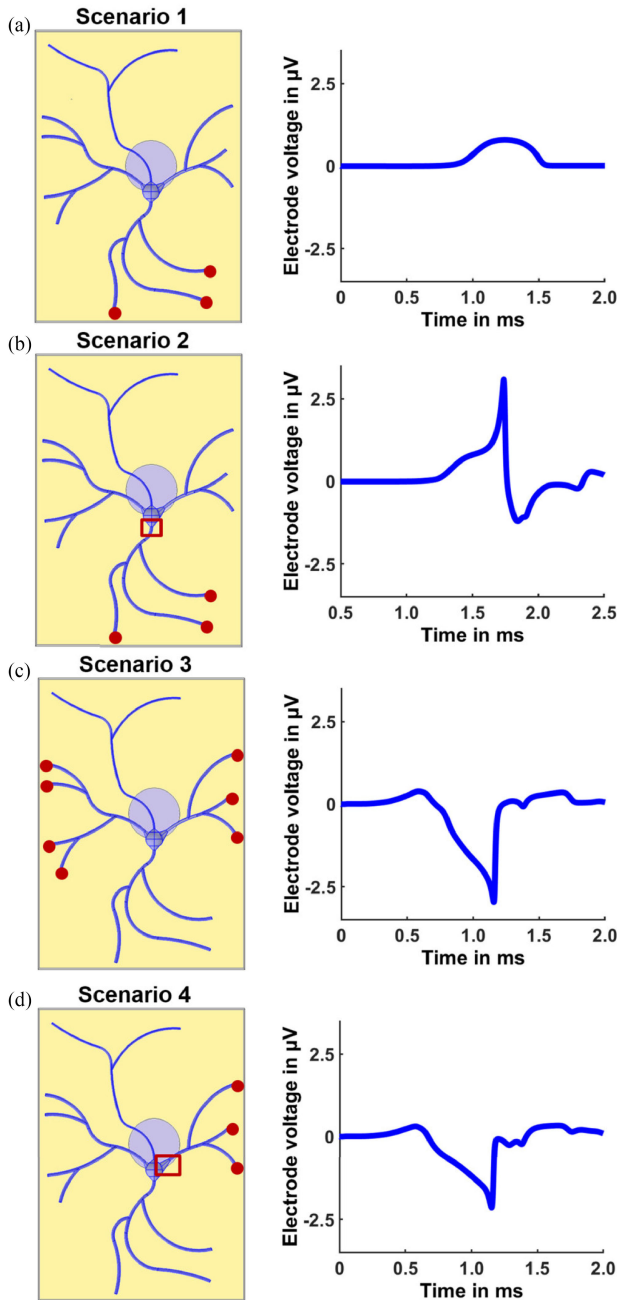


Fig. 13. Resulting electrode signals for different stimulus origins concerning neuron geometry. (a)–(b) While the initiation of the AP generation in the AIS using the apical dendrite is not achieved for the original neuron geometry, expanding the junction between apical dendrite and soma facilitates stimulation. Based on the resulting potential distribution in extracellular space, this yields an electrode signal with a positive amplitude. (c)–(d) In contrast, stimulation via the basal dendrites results in a signal trace with negative amplitude. Similar to scenario 2, see (b), an enlargement of the junction between dendrite and soma is necessary to initiate the AP generation with only a single basal dendrite.

the same dendritic input is sufficient to ensure the propagation of the AP through the soma, and hence AP-re-generation at the AIS is achieved (see Fig. 13b). In that, scenario 2 yields an electrode signal with an absolute positive amplitude of $2.5 \mu\text{V}$.

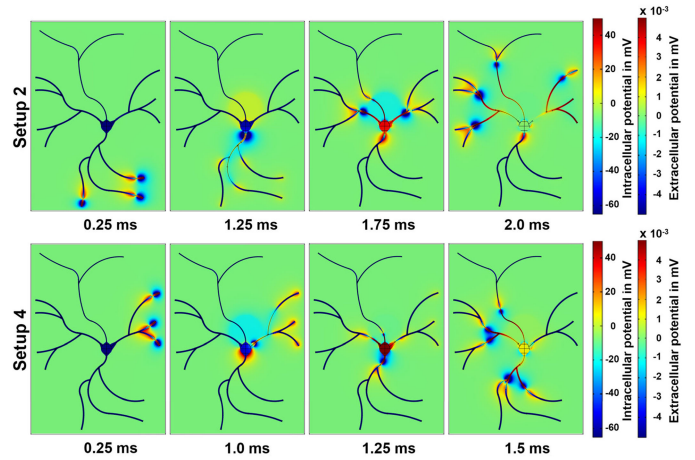


Fig. 14. Intra- and extracellular potentials of scenarios 2 and 4 (top view). The origin of the stimulus in scenario 2 yields a positive potential at the electrode surface during the depolarization of soma and AIS, followed by a less pronounced negative potential in the subsequent repolarization phase. In contrast, in scenario 4, the potential distribution near the electrode consists mainly of an initial negative potential followed by a small positive potential distribution during the repolarization of soma and AIS.

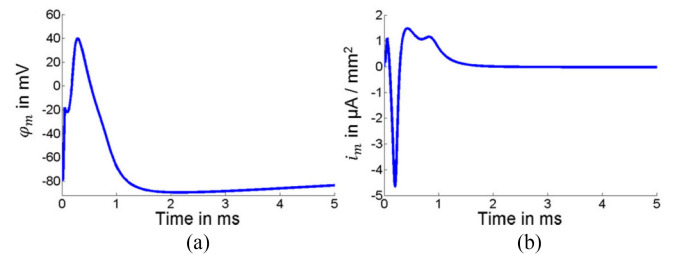


Fig. 15. Transmembrane potential φ_m and respective transmembrane current density i_m of the stimulating signal used to evoke AP-generation and -propagation for model III.

Similar to scenario 1, the dendritic AP of a single basal branch of model III is insufficient to achieve AP-propagation across the soma.

Nevertheless, with incoming evocation from both basal dendrite branches, AP-propagation, and subsequent re-generation can be achieved for scenario 3 (see Fig. 13c). In contrast to scenario 2, this yields a monopolar electrode signal with an amplitude of $-2.8 \mu\text{V}$. In scenario 4, the adaptation of the geometry at the junction of the basal dendrite facilitates AP-propagation into the soma, which allows for subsequent AP-propagation. The derived electrode signal is similar to scenario 3 but slightly reduced to $-2.3 \mu\text{V}$. The explanation for the noticeable difference between electrode signals of scenario 2 compared to scenarios 3 and 4 can be found using the extracellular potential distribution due to AP-propagation (see Fig. 14). Overall, the resulting extracellular potential distribution is similar to the results of Models I–III without AP-stimulation via dendrites (see Fig. 6).

In all these cases, AP-propagation through the soma yields a more pronounced Na^+ current at the junction of soma to AIS and an increased K^+ current near the junction to the apical dendrite (see Fig. 16). Therefore, the extracellular potential is

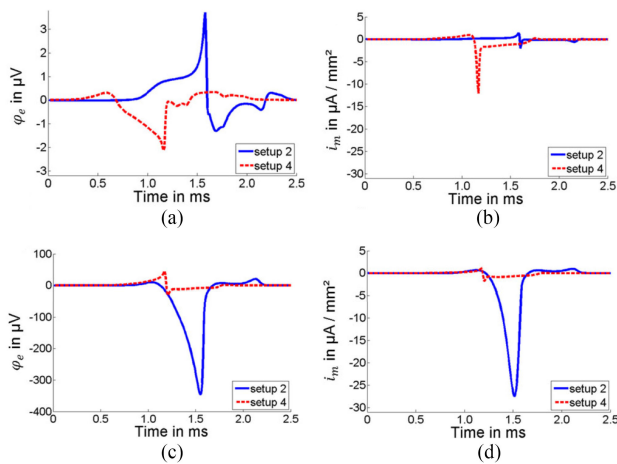


Fig. 16. Resulting extracellular potential φ_e and respective transmembrane current density i_m at the axon hillock (a) and (b) and the junction of soma and dendrite (c) and (d) for stimulation scenarios 2 and 4 based on model III.

negative near the AIS while it is positive at the junction between soma and apical dendrite.

In contrast, the distribution of the extracellular potential near the soma is reversed for scenario 2. The direction of the input potential that evokes AP-generation causes a more pronounced Na^+ current into the soma at the junction to the apical dendrite and an increased K^+ current near the axon hillock. Due to the changed distribution of the extracellular potential, this yields a substantially different electrode signal for identical recording positions.

In consequence, the location of the AP-evoking input is a vital factor that influences the resulting shape and amplitude of a derived MEA-electrode signal. Hence, this indicates that the structure of the neuronal network surrounding the measured cell may noticeably affect the result of the extracellular recording. The neuronal signal path's importance was also found in previous simulations of *in vivo* recordings presented in [10], which showed that different sites of AP initiation yielded varying shapes for the derived electrode signal.

IV. DISCUSSION

Measuring the electrical activity of neurons using MEA-electrodes can yield a variety of different signal shapes, which can significantly hamper subsequent data analysis. In this context, the goal of this model-based study was identifying and analyzing the responsible factors. Based on several FEM-models, multiple parameters with different influences on the resulting electrode signal were identified. Using model I, it was shown that parameters describing the electrical coupling between neuron and electrode primarily define the signal amplitude.

The essential parameter was found to be the cell-coverage of the electrode, which can significantly in/decrease the signal amplitude by more than one order of magnitude. In addition, cell-coverage also influences the impact of other parameters, so that, e.g., the distance between neuron and electrode becomes a critical factor in case of sufficiently dense cell-coverage. These

findings also highlight the importance of an explicit simulation of the measuring electrode in order to reproduce the effects of the neuron-to-electrode coupling accurately.

While methods like the point- and line-source approximation used in [14], [15] and [25] are suitable for an estimate of EAP at specific locations of extracellular space, such approximations do not account for interactions between the electrode and extracellular space. Other computational studies, e.g. [10], [12], [13], reproduce extracellular recording of *in vivo* or slice-based cultures with detailed electrode description, yet describe a different form of the experimental setup. Instead of a tip or shank-based electrodes, MEA-based *in vitro* setups have planar electrodes on an electrically insulated surface. Therefore, they have different properties regarding the coupling between neurons and electrodes. While results of [10], [12], [13] and of our model show qualitatively similar effects of electrode displacement on the recorded electrode signal, these effects are seen for noticeably smaller dimensions for the MEA-based *in vitro* setup of our model. Furthermore, differences between *in vitro* and *in vivo* based measurement setups regarding factors like electrode coverage should be taken into account.

In this context, as shown using model I, there is a very noticeable effect of a planar extracellular electrode on the extracellular potential for MEA-based recordings. This is because its presence alters the electric connection between the neuron, which works as a current source, and the electric reference potential as a current sink. In comparison, models using the point- and line-source approximation miss this effect as these entirely exclude the electrode from the model or only roughly describe it as an insulating surface.

Furthermore, Models I, II, and III revealed a significant dependence of the derived signal shape on the electrode position. Our model mainly confirms and refines the results shown in prior simulations in perspective with findings published in previous works. The influence of electrode shape, as well as distance and position to the recorded neuron is shown for *in vitro* setups with a more detailed 3D FEM model in comparison with previous publications (e.g. [9], [21]).

Although our findings are generally in good agreement with previous cable equation-based results [10], [12]–[15], our model offers additional degrees of freedom for describing neuron geometry and morphology. Precisely, the changes of neuron geometry due to attachment to a surface and continuous gradients of ion channel densities can be addressed using our models.

Finally, it was further shown with model III that the path of incoming signals, which are used to evoke AP-generation, is an additional factor with substantial influence and noticeably changes the shape of derived electrode signals. This is in good agreement with results shown in [10], which indicated a similar influence of signal path on the resulting extracellular recording for *in vivo* like measurement setups. Our findings suggest that the shape of the extracellular recording not only contains information about the electrical activity of the measured neuron but also regarding the neuronal activity of neighboring cells.

V. CONCLUSION

In this computational study, we investigated the influence of neuronal morphology on the shape of extracellular *in vitro* recordings with MEA. Several computational models with increasing geometrical and morphological complexity were introduced and analyzed. Both neuron and experimental setup were described in a 3D model, and a FEM-approach was used for solving. An adapted Hodgkin-Huxley model with ion channel kinetics adjusted for mammalian neurons was used to simulate AP-generation and -propagation.

Typical ion channel densities were defined at the membrane of particular neuronal subdomains, and continuous transients between subdomains were imposed. A distinct electrode description was included in the 3D model to allow for a detailed approximation of the physical interface between neuron and electrode. The connection to the subsequent measurement setup was described with a respective equivalent circuit.

Our results show that a variety of factors influence the resulting signal shape of an extracellular recording. These factors include the distance between neuron and recording electrode, the size of the electrode, and electrode coverage, which were assessed particularly for an MEA-based setup *in vitro*.

Furthermore, our models show the impact of different neuron morphologies on the electrode signal for otherwise identical electrode positions. Finally, our results confirm that different signal paths for the same neuron morphology change the shape of the signal measured by the MEA-electrode. Our findings indicate that the variety of signal shapes found in MEA-recordings originates from multiple factors. However, since the influence of these parameters is interdependent, a universal assessment seems not possible. Instead, it is necessary to simulate distinct situations found in experimental recordings to quantify the impact of a specific factor.

VI. LIMITATIONS AND OUTLOOK

Even with the detailed description of a neuron and experimental recording setup of an MEA-based *in vitro* recording presented in this work, a general overview of possible signal shapes could not be achieved. In consequence, this noticeably limits the applicability of our results on experimentally measured data. The models presented here offer a comprehensive insight into the effect of geometrical and morphological factors on the resulting electrode signal. Quantitative comparison and analysis based on the model results would only be feasible if there is no significant deviation between model and experiment.

As a result, a comparison of simulation and experimentally measured data can only yield meaningful insights, if these factors can be acquired for a specific measurement and subsequently implemented into the computational model. Due to the 3D modeling approach using FEM, such adaptations are generally unproblematic and straightforward for the models presented in this work. In order to facilitate further studies in this direction, the FEM models presented here are openly available in GitHub at <https://github.com/ra808/Influence-of-neuronal-morphology-on-extracellular-potentials-on-MEAs>.

To gain necessary information for particular pairs of neurons and electrodes, experimental setups of *in vitro* cultures using HD-MEA offer suitable methods. Information on the position and the geometric shape of the recorded neurons can be gained by fluorescence imaging and the signal path can be approximated with recordings of nearby electrodes (see e.g. [44], [45]).

This would allow for detailed validation of the presented simulation model. Furthermore, the approach of utilizing FEM with a detailed 3D description can be used for various cell shapes and types, as well as for alternative recording setups.

In perspective, complementing experimental measurement and computational modeling shows much promise to yield better insight into electrical neuron activity. It may yield new findings regarding the influence of neuron geometry and morphology on the recorded signals of single neurons inside a neuronal network culture.

APPENDIX

All three gating variables are described by a differential equation that calculates their temporal evolution concerning empirically derived functions α_k and β_k

$$\frac{dk(T)}{dt} = \theta_k(T) \alpha_k(\varphi_m) (1 - k) - \beta_k(\varphi_m) k \quad k = m, n, h \quad (\text{A1})$$

Both α_k and β_k depend on the transmembrane potential φ_m and are unique for each gating variable. The coefficient θ_k is used for temperature adaptation and calculated based on an empirical Q_{10} interval in the form of a scalar quantity as

$$\theta_k(T) = Q_{10}^{\frac{T-T_0}{10}}. \quad (\text{A2})$$

Besides, the ion-dependent permittivity g_{ion} changes with temperature

$$g_{ion}(T) = \theta_{ion}(T) g_{ion}(T_0). \quad (\text{A3})$$

Based on the Nernst-equation, the reversal potential for each ion is affected

$$E_{ion}(T) = E_{ion}(T_0) \frac{T}{T_0}. \quad (\text{A4})$$

REFERENCES

- [1] L. Berdondini *et al.*, "High-density electrode array for imaging in vitro electrophysical activity," *Biosens. Bioelectron.*, vol. 21, pp. 167–174, 2005.
- [2] F. Franke *et al.*, "High-density microelectrode array recordings and real-time spike sorting for closed-loop experiments: an emerging technology to study neural plasticity," *Front. Neural Circuits*, vol. 6, p. 105, Dec. 2012.
- [3] Y. Nam and B. C. Wheeler, "In vitro microelectrode array technology and neural recordings," *Crit. Rev. Biomed. Eng.*, vol. 39, no. 1, pp. 45–61, 2011.
- [4] M. E. J. Obien *et al.*, "Revealing neuronal function through microelectrode array recordings," *Front. Neurosci.*, vol. 9, no. JAN, p. 423, Jan. 2015.
- [5] G. R. Holt and C. Koch, "Electrical interactions via the extracellular potential near cell bodies," *J. Comput. Neurosci.*, vol. 6, no. 2, pp. 169–84, 1999.
- [6] A. Agudelo-Toro and A. Neef, "Computationally efficient simulation of electrical activity at cell membranes interacting with self-generated and externally imposed electric fields," *J. Neural Eng.*, vol. 10, no. 2, Apr. 2013, Art. no. 026019.

- [7] S. Joucla, A. Glière, and B. Yvert, "Current approaches to model extracellular electrical neural microstimulation," *Front. Comput. Neurosci.*, vol. 8, no. February, p. 13, 2014.
- [8] R. Appali, *Modeling the Coupling of Actionpotential and Electrodes*. Universität Rostock, 2013.
- [9] C. Moulin *et al.*, "A new 3-D finite-element model based on thin-film approximation for microelectrode array recording of extracellular action potential," *IEEE Trans. Biomed. Eng.*, vol. 55, no. 2, pp. 683–692, Feb. 2008.
- [10] C. Gold *et al.*, "On the origin of the extracellular action potential waveform: A modeling study," *J. Neurophysiol.*, vol. 95, pp. 3113–3128, 2006.
- [11] R. Bestel *et al.*, "Effect of morphologic features of neurons on the extracellular electric potential: A simulation study using cable theory and electro-quasi-static equations," *Neural Comput.*, vol. 29, no. 11, pp. 2955–2978, Nov. 2017.
- [12] M. A. Moffitt and C. C. McIntyre, "Model-based analysis of cortical recording with silicon microelectrodes," *Clin. Neurophysiol.*, vol. 116, no. 9, pp. 2240–2250, 2005.
- [13] S. F. Lempka *et al.*, "Theoretical analysis of intracortical microelectrode recordings," *J. Neural Eng.*, vol. 8, no. 4, 2011, Art. no. 045006.
- [14] H. Parasuram *et al.*, "Computational modeling of single neuron extracellular electric potentials and network local field potentials using LFPsim," *Front. Comput. Neurosci.*, vol. 10, 2016, Art. no. 65, doi: [10.3389/fncom.2016.00065](https://doi.org/10.3389/fncom.2016.00065).
- [15] H. Lindén *et al.*, "LFPy: A tool for biophysical simulation of extracellular potentials generated by detailed model neurons," *Front. Neuroinform.*, vol. 7, 2014, Art. no. 41, doi: [10.3389/fninf.2013.00041](https://doi.org/10.3389/fninf.2013.00041).
- [16] R. Plonsey and D. B. Heppner, "Considerations of quasi-stationarity in electrophysiological systems," *Bull. Math. Biophys.*, vol. 29, pp. 657–664, 1967.
- [17] U. van Rienen, *Numerical Methods in Computational Electrodynamics*. Berlin, Germany: Springer-Verlag, 2001.
- [18] U. van Rienen *et al.*, "Modeling and simulation of electro-quasistatic fields," in *Modeling, Simulation, Optimization Integrated Circuits*. Basel: Birkhäuser Basel, 2003, pp. 17–31.
- [19] U. Van Rienen *et al.*, "Electro-quasistatic simulations in bio-systems engineering and medical engineering," *Adv. Radio Sci.*, vol. 3, pp. 39–49, 2005, doi: [10.5194/ars-3-39-2005](https://doi.org/10.5194/ars-3-39-2005).
- [20] A. P. Buccino *et al.*, "How does the presence of neural probes affect extracellular potentials?," *J. Neural Eng.*, vol. 16, no. 2, 2019, Art. no. 026030, doi: [10.1088/1741-2552/ab03a1](https://doi.org/10.1088/1741-2552/ab03a1).
- [21] J. R. Buitengeweg, W. L. C. Rutten, and E. Marani, "Geometry based finite-element modeling of the electrical contact between a culture neuron and a microelectrode," *IEEE Trans. Biomed. Eng.*, vol. 50, no. 4, pp. 501–510, Apr. 2003.
- [22] A. L. Hodgkin and A. F. Huxley, "A quantitative description of membrane current and its application to conduction and excitation in nerve," *J. Physiol.*, vol. 117, no. 4, pp. 500–544, 1952.
- [23] Z. F. Mainen *et al.*, "A model of spike initiation in neocortical pyramidal neurons," *Neuron*, vol. 15, no. 6, pp. 1427–1439, 1995.
- [24] Y. Yu, A. P. Hill, and D. A. McCormick, "Warm body temperature facilitates energy efficient cortical action potentials," *PLoS Comput. Biol.*, vol. 8, no. 4, paper e1002456, 2012.
- [25] G. Massobrio, S. Martinoia, and P. Massobrio, "Equivalent circuit of the neuro-electronic junction for signal recordings from planar and engulfed micro-nano-electrodes," *IEEE Trans. Biomed. Circuits Syst.*, vol. 12, no. 1, Feb. 2018.
- [26] C. Nick, *Mikrointegrierte Nanostrukturen mit hohem Aspektverhältnis als neuronale Schnittstelle*. Darmstadt, Germany: Technische Universität Darmstadt, 2015.
- [27] A. Larkman and A. Mason, "Correlations between morphology and electrophysiology of pyramidal neurons in slices of rat visual cortex. I. Establishment of cell classes," *J. Neurosci.*, vol. 10, no. 5, pp. 1407–14014, 1990.
- [28] A. J. Trevelyan and J. Jack, "Detailed passive cable models of layer 2/3 pyramidal cells in rat visual cortex at different temperatures," *J. Physiol.*, vol. 539, no. Pt 2, pp. 623–636, 2002.
- [29] A. Peters and I. R. Kaiserman-Abramof, "The small pyramidal neuron of the rat cerebral cortex," *Zeitschrift für Zellforsch. und Mikroskopische Anat.*, vol. 100, no. 4, pp. 487–506, 1969.
- [30] D. Ropireddy *et al.*, "Axonal morphometry of hippocampal pyramidal neurons semi-automatically reconstructed after in vivo labeling in different CA3 locations," *Brain Struct. Funct.*, vol. 216, no. 1, pp. 1–15, 2011.
- [31] D. Braun and P. Fromherz, "Fluorescence interferometry of neuronal cell adhesion on microstructured silicon," *Phys. Rev. Lett.*, vol. 81, 1998, Art. no. 5241.
- [32] M. H. Kim *et al.*, "Neurons on nanometric topographies: Insights into neuronal behaviors in vitro," *Biomater. Sci.*, no. 2, pp. 148–155, 2014, doi: [10.1039/c3bm60255a](https://doi.org/10.1039/c3bm60255a).
- [33] F. Greve *et al.*, "Molecular design and characterization of the neuron-microelectrode array interface," *Biomaterials*, vol. 28, no. 35, pp. 5246–5258, 2007.
- [34] C. A. R. Chapman *et al.*, "Nanoporous gold biointerfaces: Modifying nanostructure to control neural cell coverage and enhance electrophysiological recording performance," *Adv. Funct. Mater.*, vol. 27, no. 3, 2017, Art. no. 1604631, doi: [10.1002/adfm.201604631](https://doi.org/10.1002/adfm.201604631).
- [35] A. R. Kriegstein and M. A. Dichter, "Morphological classification of rat cortical neurons in cell culture," *J. Neurosci.*, vol. 3, no. 8, pp. 1634–1647, 1983.
- [36] M. Rapp *et al.*, "Modeling back propagating action potential in weakly excitable dendrites of neocortical pyramidal cells," in *Proc. Natl. Acad. Sci.*, vol. 93, no. 21, pp. 11985–11990, 1996.
- [37] C. Bernard and D. Johnston, "Distance-dependent modifiable threshold for action potential back-propagation in hippocampal dendrites," *J. Neurophysiol.*, vol. 90, no. 3, pp. 1807–18016, 2003.
- [38] Y. Buskila *et al.*, "The adaptation of spike backpropagation delays in cortical neurons," *Front. Cell. Neurosci.*, vol. 7, 2013, Art. no. 192, doi: [10.3389/fncel.2013.00192](https://doi.org/10.3389/fncel.2013.00192).
- [39] F. Amzica and M. Steriade, "Neuronal and glial membrane potentials during sleep and paroxysmal oscillations in the neocortex," *J. Neurosci.*, vol. 20, no. 17, pp. 6648–6665, 2000.
- [40] S. Jäkel and L. Dimou, "Glial cells and their function in the adult brain: A journey through the history of their ablation," *Front. Cellular Neurosci.*, vol. 11, pp. 1–24, 2017, doi: [10.3389/fncel.2017.00024](https://doi.org/10.3389/fncel.2017.00024).
- [41] M. Montal and P. Mueller, "Formation of bimolecular membranes from lipid monolayers and a study of their electrical properties," in *Proc. Natl. Acad. Sci.*, vol. 69, no. 12, pp. 3561–3566, 1972, doi: [10.1073/pnas.69.12.3561](https://doi.org/10.1073/pnas.69.12.3561).
- [42] P. J. Koester *et al.*, "Modular glass chip system measuring the electric activity and adhesion of neuronal cells - Application and drug testing with sodium valproic acid," *Lab Chip*, vol. 10, no. 12, pp. 1579–1586, 2010.
- [43] P. Vetter, A. Roth, and M. Hausser, "Propagation of action potentials in dendrites depends on dendritic morphology," *J. Neurophysiol.*, vol. 85, no. 2, pp. 926–937, 2001.
- [44] J. Müller *et al.*, "High-resolution CMOS MEA platform to study neurons at subcellular, cellular, and network levels," *Lab. Chip*, no. 13, pp. 2767–2780, 2015, doi: [10.1039/c5lc00133a](https://doi.org/10.1039/c5lc00133a).
- [45] D. Jäkel *et al.*, "Combination of high-density microelectrode array and patch clamp recordings to enable studies of multisynaptic integration," *Sci. Rep.*, vol. 7, 2017, Art. no. 978, doi: [10.1038/s41598-017-00981-4](https://doi.org/10.1038/s41598-017-00981-4).